Deep-Sea Research II, Vol. 40, No. 1/2, pp. 9–35, 1993.
Printed in Great Britain.

0967–0645/93 $5.00 + 0.00

Mesoscale and upper ocean variabilities during the 1989 JGOFS bloom study

A. R. ROBINSON,* D. J. MCGILLICUDDY,* J. CALMAN,† H. W. DUCKLOW,‡ M. J. R. FASHAM,§ F. E. HOGE,‖ W. G. LESLIE,* J. J. MCCARTHY,* S. PODEWSKI,¶ D. L. PORTER,† G. SAURE¶ and J. A. YODER**

(*Received* 13 *May* 1991; *in revised form* 3 *March* 1992; *accepted* 20 *March* 1992)

Abstract—Altimetric data from Geosat and some critical hydrographic measurements were used to estimate in real time the mesoscale physical oceanographic environment surrounding the Joint Global Ocean Flux Study (JGOFS) 1989 North Atlantic Bloom Experiment. Three cyclonic eddies, including an exceptionally large one, evolved and interacted over the 10 weeks of observations. Subsequent analysis of all available hydrographic data confirmed the real time estimates and provided further quantitative information concerning the mesoscale and submesoscale structure of the upper ocean. Remotely sensed indicators of near-surface chlorophyll content reveal significant biological variability on these wavelengths. The altimetric and hydrographic data have been assimilated into a dynamical model to produce optimal estimates of physical fields of interest as they evolve in time for use in physical and biological process studies.

INTRODUCTION

IN 1989 the Joint Global Ocean Flux Study (JGOFS) program staged a multinational coordinated effort to investigate the spring phytoplankton bloom in the North Atlantic along longitude 20°W from 15 to 60°N (DUCKLOW, 1989). One of the most intensively sampled locations on this transect was the 47°N site, which was occupied from late April until mid-June, with other stations in July–August. During this time, a combination of altimetric data from Geosat and *in situ* observations was used to define in real time the mesoscale flow field in an approximately 500 km^2 region in the vicinity of the experiment.

Satellite altimetry has emerged as a powerful tool in the remote sensing of oceanic currents, fronts and eddies. By measuring the distance from the satellite to the sea surface

*Department of Earth and Planetary Sciences, Harvard University, Cambridge, MA 02138, U.S.A.
†The Johns Hopkins University Applied Physics Laboratory, Laurel, MD 20723, U.S.A.
‡Horn Point Laboratory, University of Maryland, CEES, P.O. Box. 775, Cambridge, MD 21613, U.S.A.
§James Rennell Centre for Ocean Circulation, Gamma House, Chilworth Research Centre, Chilworth, Southampton SO1 7NS, U.K.
‖NASA Goddard Space Flight Center, Wallops Flight Facility code 972, Wallops Island, VA 23337, U.S.A.
¶Institut Für Meereskunde an der Universität Kiel, Dusternbrooker Weg 20, D-2300 Kiel 1, Germany.
**Graduate School of Oceanography, University of Rhode Island, Narragansett, RI 02882, U.S.A.

along a trajectory, an altimeter can provide valuable information concerning deformations in sea surface height associated with mesoscale flow features (CALMAN, 1987; WUNSCH and GAPOSCHKIN, 1980). However, it is usually essential to have some critical *in situ* data for interpretation of the altimetric signal (PORTER *et al.*, 1989). Assimilation of these data into a dynamical model of regional ocean physics provides dynamical interpolation and forecasts of the flow field. A nowcast and forecast system, consisting of an assimilating scheme for altimeter sea surface height and critical *in situ* data into a dynamical model, can be used to derive optimal four-dimensional field estimates. Knowledge of such fields via first estimates in real time can be very helpful for the design of physical and biological sampling strategies and the conduct of experiments at sea (CALMAN and MANZI, 1989; ROBINSON, 1986; ROBINSON *et al.*, 1989). Improved realizations of the four-dimensional flow field via analyses and hindcast simulations can provide a necessary context in which to interpret the observed biological variability and to analyze biological dynamics.

Mesoscale oceanic features can influence biological processes in a variety of ways. The perturbation of density surfaces associated with these flows can significantly alter the availability of nutrients in the euphotic zone (NELSON *et al.*, 1989). Moreover, bursts of dynamical activity (such as frontogenesis, eddy interactions, etc.) can give rise to substantial vertical velocities in localized regions (WOODS, 1988). In addition to the above two vertical advective processes, interaction between the mesoscale and the surface boundary layer can produce spatial and temporal variability in both the rate and extent of vertical mixing in the upper ocean. Finally, all of these processes occur in a continuously evolving environment in which the biological fields of interest are deformed, rearranged and advected by the flow. In many cases, plankton communities trapped within eddies can be transported quite far from their place of origin (ANGEL and FASHAM, 1983).

Prior observations in the area of interest in the Northeast Atlantic have revealed the existence of mesoscale eddies with varying characteristics. Using hydrographic measurements, current meters and floats, LE GROUPE TOURBILLION (1983) documented an anticyclonic eddy of radius 50–70 km near 47°N, 15°W. Maximum velocities inside the eddy were on the order of 30 cm s^{-1}. Both cyclonic and anticyclonic eddies of similar dimension and strength were observed with hydrographic and altimetric measurements in the AthenA experiment at 52°N, 25°W (ATHENA GROUP, in preparation). Data from the altimeter indicated sea surface height perturbations on the order of 20 cm. This region is also known to contain more intense cyclonic features apparently formed from meanders of the Polar Front (KUPFERMAN *et al.*, 1986; MITTELSTAEDT, 1987). Significant biological and chemical variability associated with these features has been observed (LOCHTE and PFANNKUCHE, 1987). The vertical displacement of the temperature surfaces inside such eddies has been observed on occasion to be in excess of 300 m. Geostrophic calculations referenced to 1500 m indicate maximum swirl velocities near 40 cm s^{-1}, approximately 35–55 km from the eddy center. The features described above are mostly comprised of proximate water masses (North Atlantic Central Water, Subarctic Intermediate Water, and North Atlantic Deep Water), with traces of water from more distant origins (Labrador and Mediterranean). However, SCHAUER (1989) reports observations of an isolated cyclonic submesoscale vortex composed almost entirely of Mediterranean water at 47°N, 20°W. The horizontal extent of the feature was approximately 75 km. The subsurface anomalous water extended down about 2400 m and maximum velocities of 15 cm s^{-1} occurred at 1570 m. Thus, although not yet well explored, from the available data the physical environment in this region appears populated with interesting phenomena.

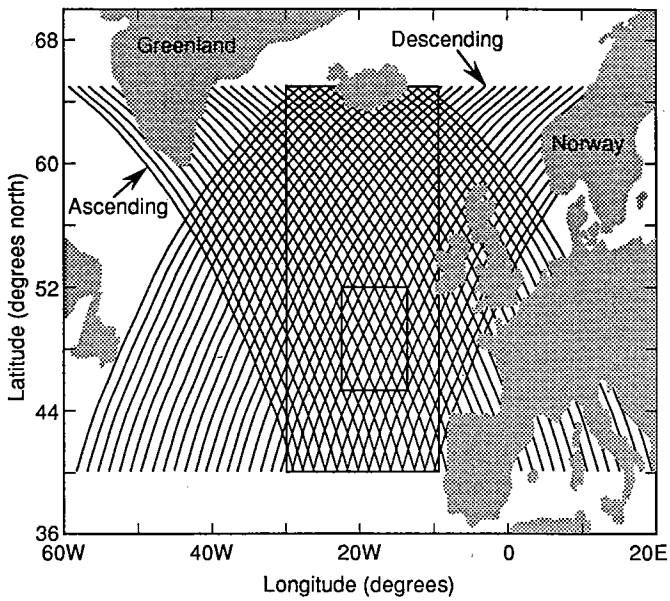

Fig. 1. A map of the Northeast Atlantic showing ascending and descending Geosat ground tracks. The area in which the altimeter mean was computed is indicated by the large rectangle. The eddy mapping domain is bounded by the smaller rectangle.

ALTIMETRIC DATA TREATMENT AND METHODOLOGY

For the purposes of this experiment, Geosat data were collected and analyzed in an area from 10–30°W, 40–65°N (Fig. 1). This cycle is completed once every 17.05 days. The altimetric signal measured by Geosat is made up of contributions from the geoid (~10 m), orbit error (~1 m), environmental corrections (~1 m), and measurement error (~5 cm) in addition to the variations in sea surface height due to oceanic features of interest (~10 cm). Thus, in order to derive an estimate of the sea surface height anomaly due to mesoscale flows, the other quantities must be eliminated. Corrections for environmental effects are made by using models of the tides, troposphere and ionosphere after the method described by PORTER *et al.* (1989). Long wavelength components of the geoid, orbit error and the large scale ocean signal are simultaneously removed from each pass by subtracting the least-squares fit of a quadratic equation to the pass relative to a reference pass. Construction of a time average of many measurements for each ground track yields a composite that contains the geoid at medium scales and any medium scale mean oceanographic signal (and the orbit error from a reference pass). Previous experience with Geosat data has shown that in the absence of a strong sub-basin scale component of the mean oceanographic signal, the altimetric mean can be removed from an individual pass to yield a good estimate of mesoscale dynamic topography (GLENN *et al.*, 1991). Analysis of climatological hydrographic data from the coarse resolution NODC data set (LEVITUS and OORT, 1977), for the present region does not indicate any strong sub-basin scale variations in the sea surface. Such features can arise from the rectified mean of the mesoscale variability, and the statistics of resolved synoptic mesoscale realizations are usually required. However, this technique has been used successfully in the nearby AthenA domain

(ATHENA GROUP, in preparation; PORTER *et al.*, 1989), where comparison of dynamic topography derived from such altimetric measurements and absolute sea surface heights computed from deep hydrographic data and floats showed good agreement. Thus it is reasonable to expect that this method is suitable for the present area of interest, and that features with amplitude greater than the 5 cm measurement error should be distinguishable from the noise.

An altimetric mean for each ground track in the area of Geosat data collection was computed using 2 years of observations from November 1986 through November 1988. Ideally there would be 44 individual passes along each ground track. However, due to off nadir satellite pointing and subsequent loss of data acquisition, in some cases as few as 35 complete passes were available. In computing the mean, the same altimetric height corrections for the ionosphere, the wet and dry troposphere and the global tides were included in the analysis as has been described previously.

Dynamic topography derived from Geosat altimetry was made available using a real-time system described by CALMAN and MANZI (1989). The methodology allows for the use of partial tracks within the domain. These tracks are shorter than the 3300 km passes used in computing the mean. Hence, the resulting alongtrack sea surface height signal can be offset by an amount as large as the large scale ocean signal (which is unknown). For this reason it is essential to have some *in situ* data to identify the proper level of the mean sea surface.

ALTIMETRIC ESTIMATION OF THE VARIABILITY OF THE REGION

The mean variability

In order to help characterize and quantify the mesoscale environment in the area, the root mean square (rms) variance of the difference in the sea surface height from the mean was calculated for the 2 years of data used in computing the altimetric mean. Figure 2 shows a map of the rms variance for the large region indicated in Fig. 1. This field is composed of 1 degree square boxes and represents the rms difference of all the measurements (typically 1000 points per square) relative to their corresponding altimetric mean sea surface. The variability is generally quite small. Over half the area in the map has an rms variability of <8 cm. Only small regions show values >10 cm and there are no areas where the variability is >12 cm except near the continental shelf, where coastal effects produce tidal signals that are not resolved by the present tidal model. This analysis is consistent with an eddy field containing an abundance of features similar to those observed in previous data sets rather than occasional isolated eddies.

The synoptic variability: 21 *April–7 May* (*year days* 117–127)

The locations of the three cyclones ("Big", "Standard" and "Small") identified in the first eddy report sent out to the JGOFS research ships at sea on 9 May are indicated in Fig. 3. Alongtrack sea surface height estimates for the five passes identifying these features are shown in Fig. 4. The mesoscale signal shows eddy-like oscillations with peak-to-trough excursions as large as 25 cm. Because the location of the mean sea surface in each pass for the small arc is not known *a priori*, it is not possible to determine the sense nor the amplitude of departures from the mean in the altimetric signal. It is therefore necessary to

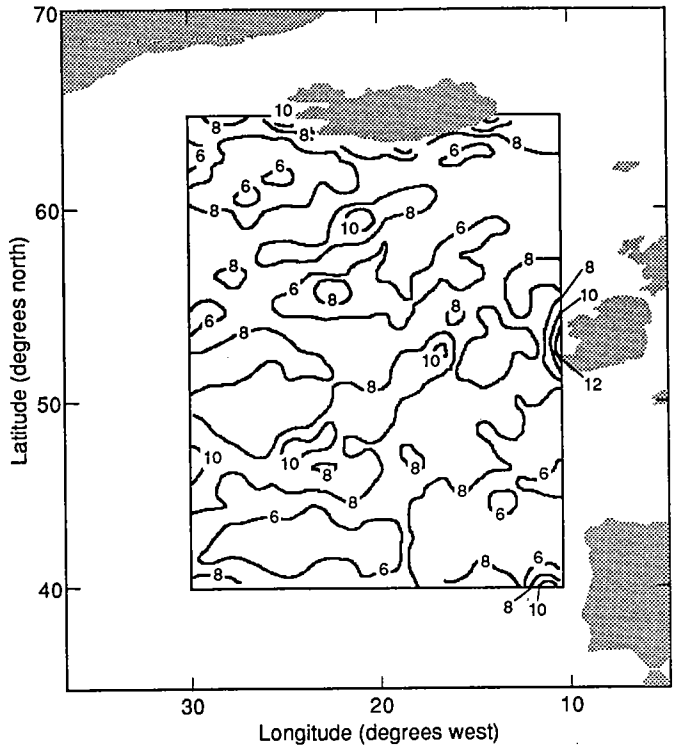

Fig. 2. Root mean square mesoscale area surface height variability (cm) of the large domain shown in Fig. 1.

begin with an analysis of track 122b, for which there was a simultaneous AXBT underflight. Although the temperature section derived from the AXBT data (Fig. 5) appears noisy the data do contain valuable information on the general location of the major eddy features. Quality control and signal extraction on small scales has not been possible or attempted. Dramatic lifting of the temperature surfaces at the northernmost station (Fig. 5) indicates the existence of a strong cyclonic feature. Although a one-probe feature, it correlates with the substantial mesoscale feature unambiguously appearing on the Geosat topographies, which is why we believe it to be the Big eddy signal. A weaker rise in the contours in Stas 3–5 suggests the presence of another cyclone. This signal of the Standard eddy should be noted particularly in the deeper data (e.g. in the 11.6 and 11.8°C isotherms). The mean sea surface of track 122b was therefore chosen as indicated in Fig. 4a to make the SSH estimate qualitatively consistent with the *in situ* observations. Taken together, these data suggest that along track 122b the Big eddy is bounded at approximately 48.4 and 50.5°N and that the Standard eddy is crossed from about 47 to 47.8°N. Having identified these two depressions in the sea surface, it is possible to piece together a map of the nearby mesoscale environment. Tracks 116b and 119b (Fig. 4b,c) define the extent of the Standard eddy and the northwest boundary of the Big eddy. Ascending track 117d provides another crossing of the Standard eddy and evidence of the depression in the sea surface associated with the Small eddy. Track 125c (Fig. 4e) indicates the southeastern boundary of the Big eddy as well as the northeast to southwest extent of the Small eddy.

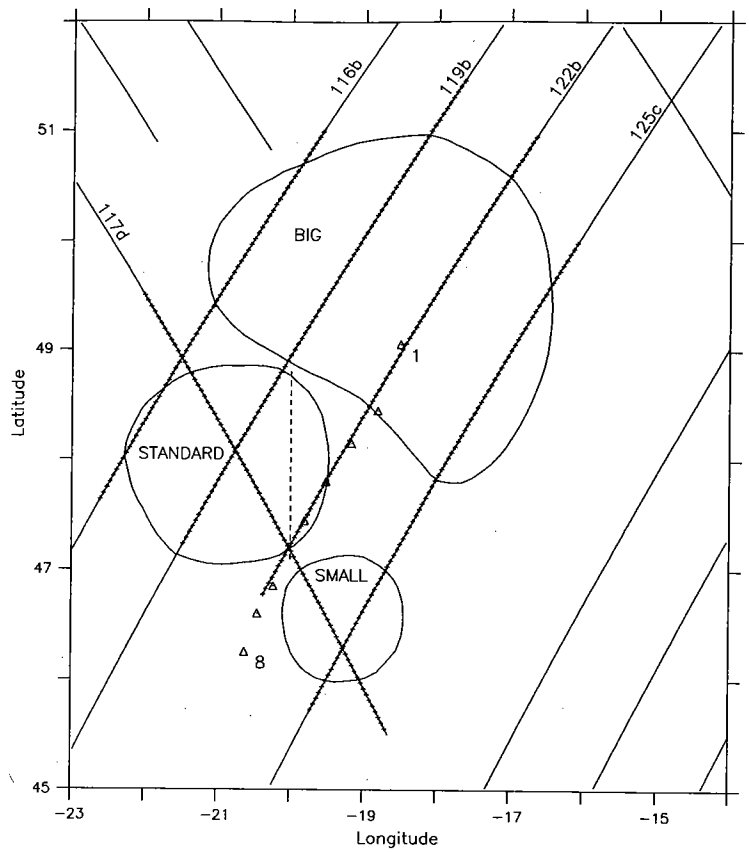

Fig. 3. Feature locations and Geosat passes available in the eddy mapping region for the period from 21 April to 7 May. Passes are identified by the number adjacent to each track which indicates the year day on which the track was occupied. Triangles represent the positions of AXBT drops. Station identifiers are shown adjacent to the northernmost and southernmost stations. Hatching on the ground tracks show the extent of the altimeter data shown in Fig. 4. Also shown is the flight track for the remotely sensed chlorophyll measurements described in the Mesoscale Biological Variability section (dashed line).

The synoptic variability: 8–24 *May* (*year days* 128–144)

During the course of the experiment, the eddy field evolved (Fig. 6). Although the depressions associated with the Standard and Big eddies persist, there is some evidence for propagation and there is noticeable temporal variability and interaction between the features.

An analysis of the altimetric and hydrographic data during the second 17-day repeat cycle is shown in Fig. 7. The first estimate of this analysis was sent out to the JGOFS research fleet on 16 May as the second eddy report, which contained the essential eddy features. In this realization the Big eddy has distorted somewhat. Additional spatial coverage of Geosat data indicated that the northwest to southeast extent of the Big eddy was substantially larger than previously believed. Some evolution was noted in the

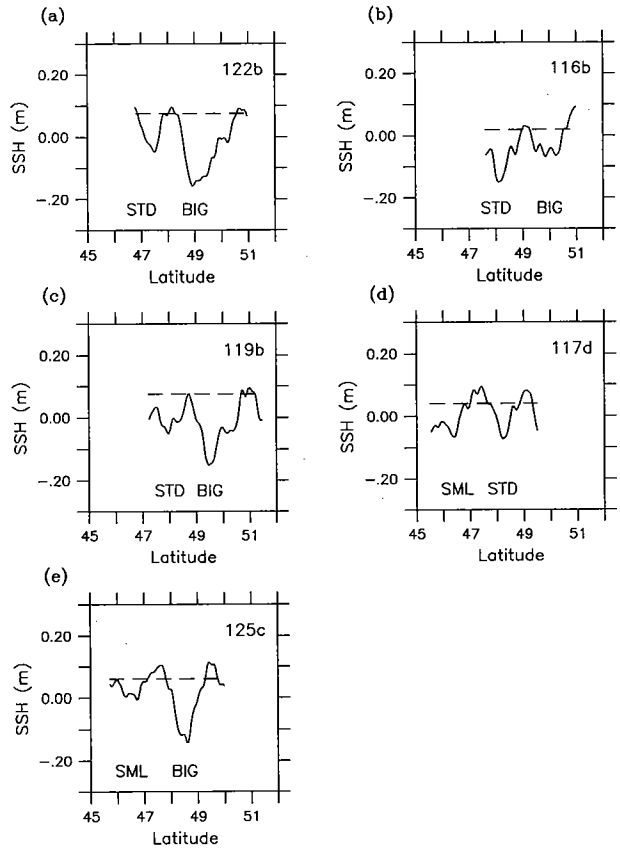

Fig. 4. Alongtrack sea surface height estimates from Geosat for the five passes identifying features in the first eddy report. The plots show the altimeter data only where indicated by hatching on the ground tracks shown in Fig. 3. Dashed lines indicate the subjectively chosen mean sea surface in each case. (a) Track 122b; (b) track 116b; (c) track 119b; (d) track 117d; (e) track 125c.

Standard eddy, and there appeared to be another feature interacting with the Small eddy to the east.

Vertical sections of temperature (Fig. 8) constructed from the three legs of a dedicated AXBT flight help to discern the structures of the Big and Standard eddies. In this region the main thermocline extends down to about 1500 m. Examination of individual profiles shows that its structure begins anywhere from 100 to 300 m. Thus the 300 m probes are just adequate to define the overall features of the main eddies. Again, quality control and signal extraction on small scales have not been possible or attempted. Also, the eddies are interpreted again from the general behavior of the deeper data. In the first leg (Fig. 8a), we interpret probes 1–14 as indicating the Big eddy. Although there is a great deal of small-scale structure in the section, the next significant displacement of the isotherms occurs at Sta. 15, where they are depressed in between the Big and Standard cyclones. The isotherms rise again at the next station upon entrance into the Standard eddy. The minor depression in the contours of temperature at Sta. 19 could be interpreted as a distortion of the eastern boundary of the Standard eddy. Leg 2 (Fig. 8b) provides a cross section of the

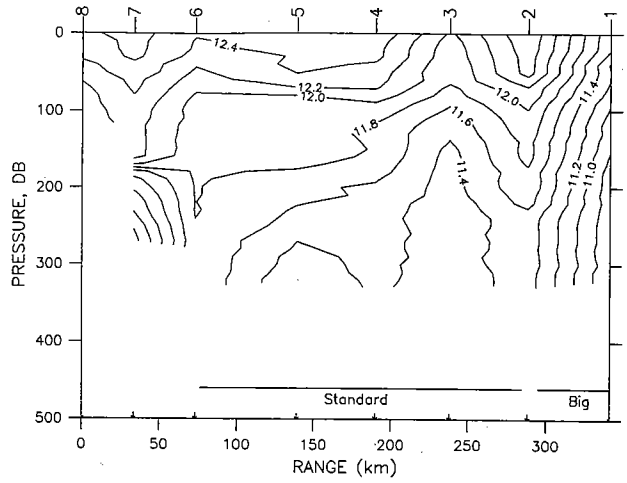

Fig. 5. Vertical section of temperature derived from AXBT measurements shown in Fig. 3. Station identifiers are shown on the top axis.

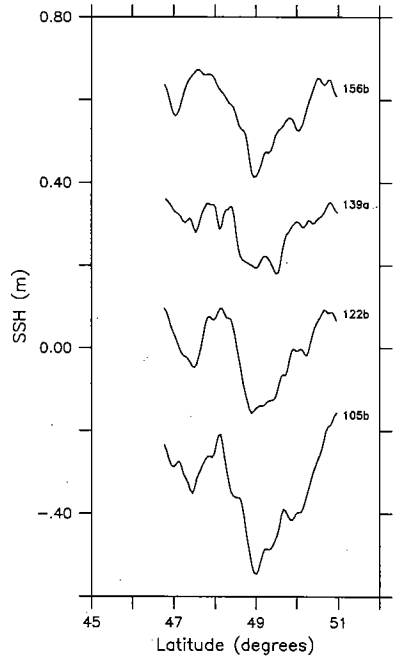

Fig. 6. A time-series of alongtrack sea surface height for the central descending track (track 122b in Fig. 3). Numbers adjacent to each track indicate the year day on which the pass occurred.

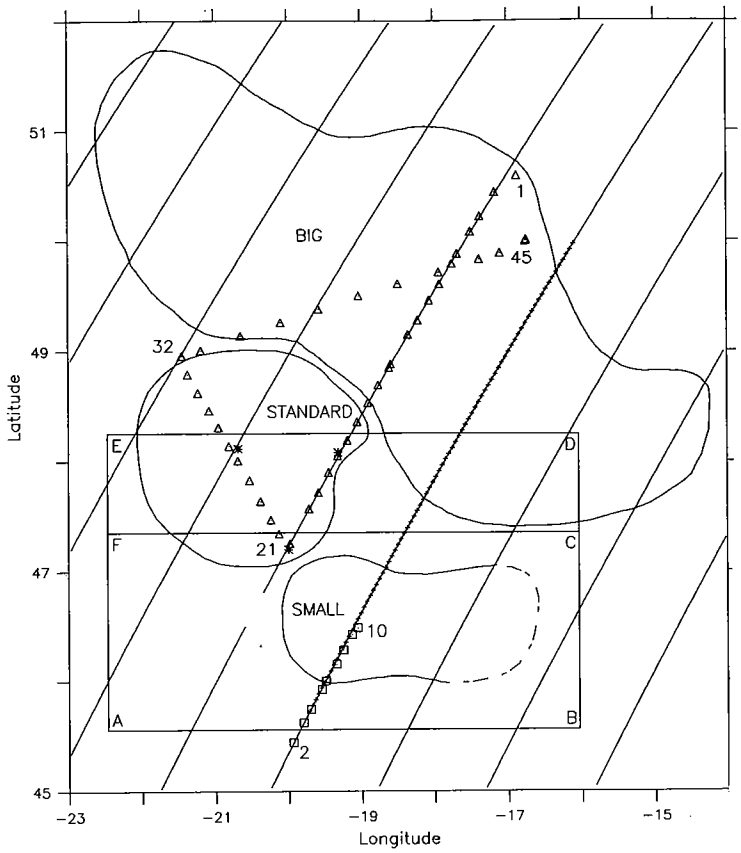

Fig. 7. Geosat passes available in the eddy mapping region for the period 8–24 May. Triangles correspond to the positions of AXBT drops for Legs 1–3, and squares to R.V. *Atlantis II* XBTs. Station identifiers are shown adjacent to section endpoints. Asterisks indicate the end points of R.R.S. *Discovery* SeaSoar sections. The objective analysis domains ABDE and ABCF discussed in the Hydrographic Data Analysis section are also shown.

Standard eddy and identifies its northwestern boundary. There are many data gaps in Leg 3 (Fig. 8c), but the boundary between the Standard and Big eddies appears to be between Stas 32 and 37.

A series of XBT measurements were made by R.V. *Atlantis II* along a Geosat track crossing the southern boundary of the Small cyclone (Fig. 7). These data were calibrated in two steps. First, a uniform stretching factor of 1.065 was applied to the depth records to correct for an inaccuracy in the drop rate equation, which has been examined by HANAWA and YOSHIKAWA (1991) and is still under investigation. Second, comparison of XBT temperature profiles with simultaneous CTD measurements showed a consistent 1.2 degree offset between the two that was most likely due to an error in the calibration of the instrument. With a 1.2 degree adjustment to each temperature record in the XBT trace, the rms difference between the two profiles over the entire depth interval was reduced to 0.14 degrees. A vertical section of temperature (Fig. 9) constructed from the calibrated XBT data shows the gentle lifting of temperature surfaces in Stas 3 and 4 with a distinct

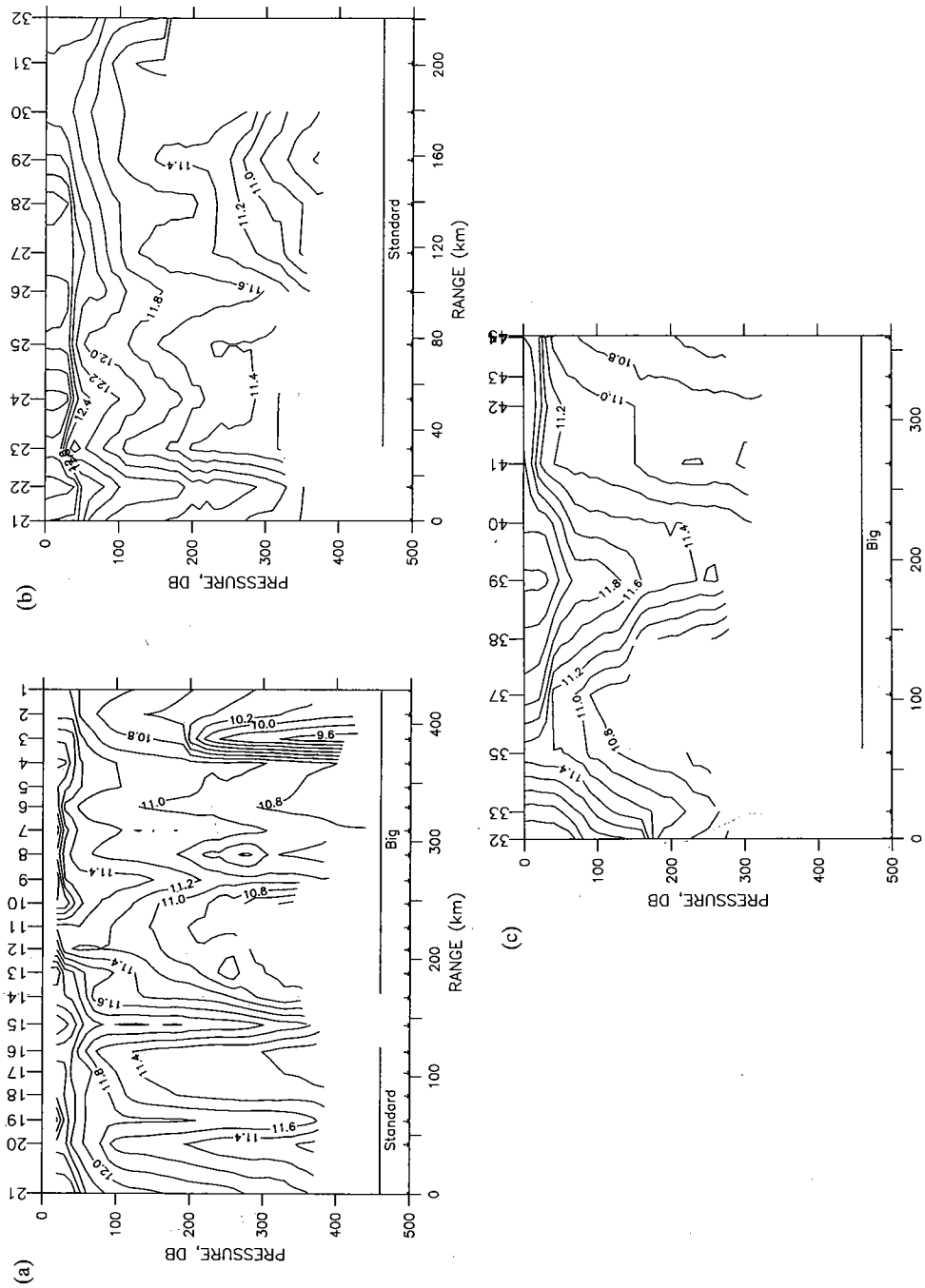

Fig. 8. Vertical sections of temperature derived from AXBT measurements shown in Fig. 7. Station identifiers are indicated on the top axis. (a) Leg 1; (b) Leg 2; and (c) Leg 3.

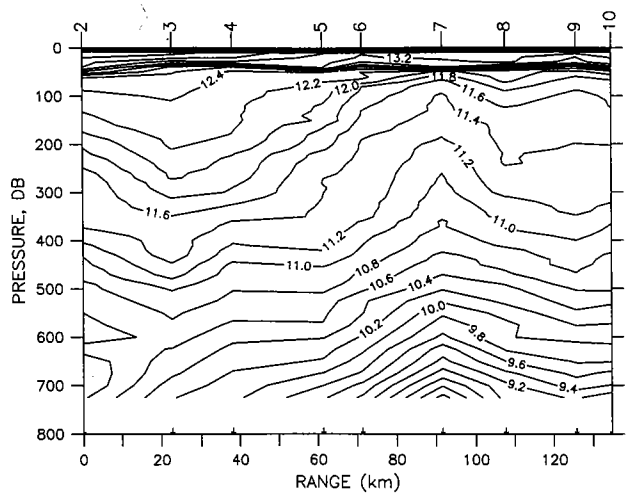

Fig. 9. Vertical section of temperature derived from XBT measurements shown in Fig. 7. Station identifiers are indicated on the top axis.

boundary near Stas 5 and 6 where the isotherms rise upon entrance into the core of the Small eddy. The isotherms then dip slightly in Stas 8 and 9 but rise again at Sta. 10, suggesting the presence of secondary circulations inside the eddy. Alongtrack dynamic height referenced to 750 m computed from the XBT data using a climatological temperature–salinity relationship shows good agreement with the altimetric signals

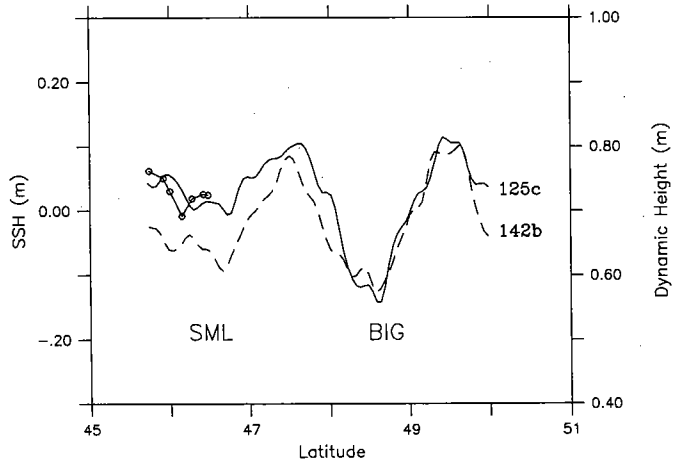

Fig. 10. Comparison of alongtrack altimetric SSH and dynamic height calculated from XBT measurements. The solid line shows SSH estimates for the bold part of track 125c indicated in Fig. 3, and the dashed line shows SSH estimates for the bold part of track 142b shown in Fig. 7. Circles show dynamic height computed from alongtrack XBT measurements taken on day 136. Note the offset vertical scales.

(Fig. 10) from the tracks occupied before (track 125c on 5 May) and after (track 142b on 22 May) the measurements were taken.

HYDROGRAPHIC DATA ANALYSIS

The near-surface region is a very complicated part of the ocean that is driven by essentially three different mechanisms. First, exchange with the atmosphere can result in significant fluxes of heat and momentum and sometimes salt. Second, disturbances in the main thermocline associated with mesoscale flows penetrate vertically into the near surface region. Finally, the interaction of these two mechanisms also produces variability of different types. Thus, in order to understand the observed property distributions, we have taken the approach of first identifying the deep eddy features and then examining the shallower regions in this context.

A substantial amount of hydrographic information from several sources was available in the region of study, including CTDs from F.S. *Meteor* and R.V. *Atlantis II* along with SeaSoar sections from R.R.S. *Discovery*. In order to produce a unified analysis of the area, it was necessary to compare and intercalibrate the various data sets. Measurements from simultaneous CTD casts taken by F.S. *Meteor* and R.V. *Atlantis II* at an intercalibration station agreed within reasonable limits of accuracy (0.01 K for temperature and 0.01 psu for salinity). The R.R.S. *Discovery* SeaSoar data were independently calibrated using reversing thermometers and salinometer analyses of water samples to achieve the same level of accuracy.

The combined data sets were then mapped onto a regular grid using objective analysis (CARTER and ROBINSON, 1987). In this technique, the best estimate and expected error of a scalar quantity at a given location are computed using a linear combination of the observations that are most highly correlated to the analysis point. In this case the correlation function is assumed to be of the form

$$c(\Delta x,\Delta y) = \left(1 - \frac{\Delta x^2}{L^2} - \frac{\Delta y^2}{L^2}\right) \exp\left(-\frac{\Delta x^2}{L^2} - \frac{\Delta y^2}{L^2}\right),$$

where $L = 60$ km. A time-dependent correlation function was not needed because of the way the temporal aspects of the data were treated in the analysis (see below).

For mapping purposes, the hydrographic observations are conveniently separated into two distinct data periods: year days 115–137 and 138–151. The upper panel in Fig. 11 shows an objectively analyzed map of dynamic height at 25 m relative to 490 m for the first period in the domain denoted ABCF in Fig. 7. The middle panel shows the expected error field for the analysis and the locations of the observations. Geostrophic velocity vectors computed from the dynamic height field are displayed in the lower panel. Because these velocities are relative to an assumed level of no motion at 490 m, they do not reflect the full strength of the total geostrophic shear. But, these data are very useful for describing the upper main thermocline contribution to the structure of the total velocity field.

The southward flow in region A (Fig. 11a) is the western edge of the Small eddy. Some 50–75 km to the east (region B) the flows turns northward. This northward transport does not appear sufficient to balance the flow on the western flank of the eddy; therefore we conjecture that the eastern border of the Small eddy lies to the east of sampling area. Just to the west of the Small eddy there is a small scale anticyclone (region C). Even farther to the west (region D) there is evidence of another cyclonic feature.

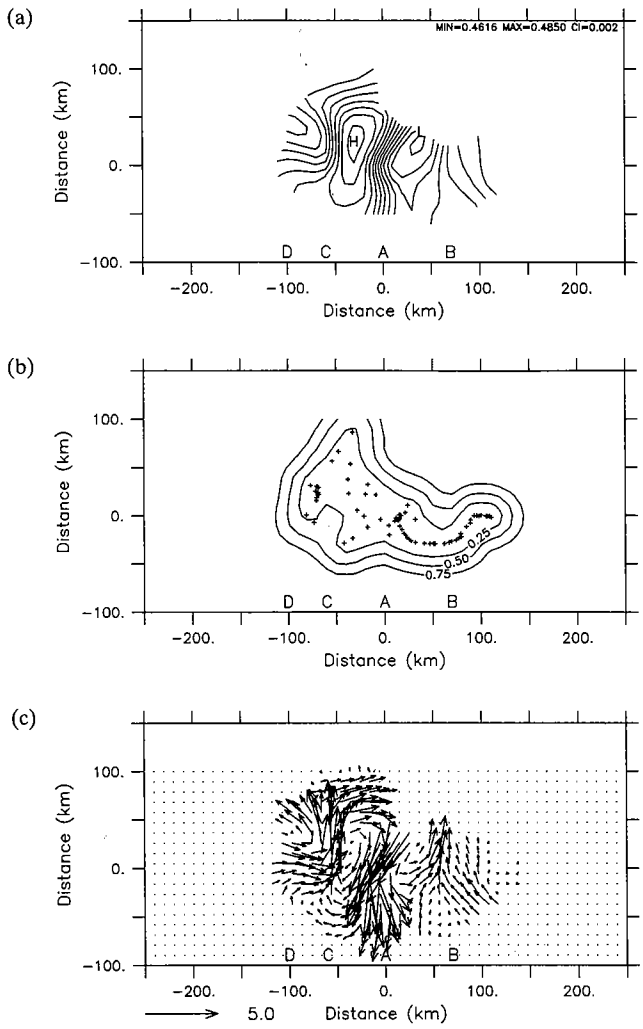

Fig. 11. (a) Objectively analyzed dynamic height at 25 m relative to 490 m for the first data period. The field has been masked where expected error exceeds 50%. The letters A–D indicate locations of important features (see text). The minimum and maximum values in the field and the contour interval are listed in the upper right portion of the panel. The locations of the high and the low values are indicated by the *h* and *l* in the field. (b) Expected error map for the above field. Locations of observation points are indicated by plus signs. (c) Geostrophic velocity vectors computed from the dynamic height field. Note the velocity scale (in cm s^{-1}) at the bottom left.

Maps of dynamic height, expected error and geostrophic velocity for the second period are shown in Fig 12a–c. In this realization the western edge of the Small eddy appears quite similar to that of the first period (region A). In contrast, the northward flow in region B is significantly stronger, with noticeable eastward flow just to the east. This feature could be the eastern flank of the Small eddy if that boundary had propagated to the west. Alternatively, this could be a secondary circulation in the interior of the eddy. From these data it is not possible to make this distinction. The western anticyclone observed in the first

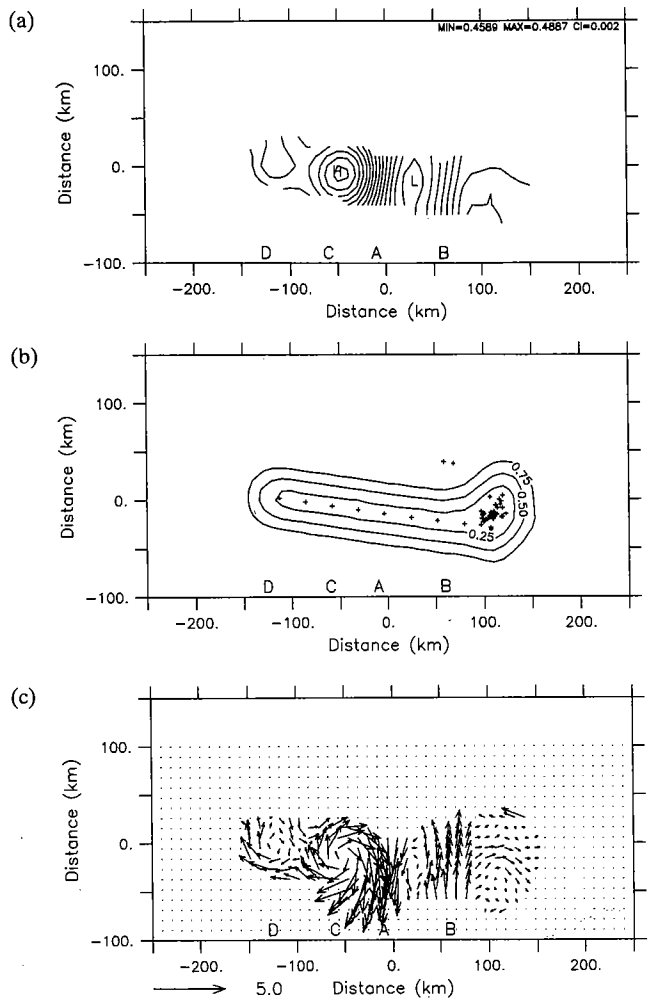

Fig. 12. (a) Objectively analyzed dynamic height at 25 m relative to 490 m for the second data period. The field has been masked where expected error exceeds 50%. The letters A–D indicate locations of important features (see text). (b) Expected error map for the above field. Locations of observation points are indicated by plus signs. (c) Geostrophic velocity vectors computed from the dynamic height field. Note the velocity scale (in cm s^{-1}) at the bottom left.

period is again evident in region C. However, the cyclonic feature in region D during the first period is not sampled in the second period. The two casts taken just to the south of region D in the second period suggest the presence of an anticyclonic feature, but there is no evidence that the cell of circulation is closed. The appearance of a closed cell in the velocity field is simply an artifact of the objective analysis technique in a data sparse region.

The section of temperature constructed from the observations between regions B and D shows the vertical structure of these features (Fig. 13). The western boundary of the Small eddy is clearly visible in the lifting of the isotherms between Stas 284 and 283. The

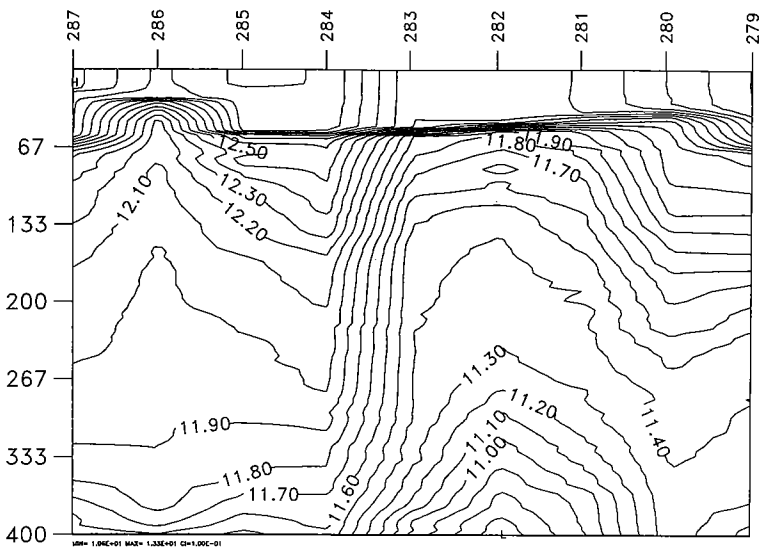

Fig. 13. Vertical section of temperature constructed from the line of observations from regions B to D in the second data period. Station identifiers are indicated on the top axis.

northward return flow is created by the subsequent dropping of isotherms between Stas 281 and 280. Isotherms in this depth range are displaced by as much as 100 m, and it appears that this feature extends down into the main thermocline. In contrast, the western anticyclone (Stas 287–285) is confined to the upper 300 m.

Objective maps of larger horizontal extent for the first data period can be constructed by incorporating information from three SeaSoar sections occupied to the north and west of the previously described features. Figure 14a–c shows the fields of temperature at 25 and 200 m and the corresponding error estimates for the domain ABDE shown in Fig. 7. The southern boundary of the Standard eddy (region E) and its proximity to the western flank of the Small eddy (region A) are quite evident in the 200 m temperature map. Comparison with the shallower field shows a significant variation in the horizontal structure with depth. At 25 m, the east–west temperature front associated with the Standard eddy appears to be displaced to the south (region F) and runs nearly north–south in the eastern part of the contoured field (region G). In addition, the temperature gradient associated with the western swirl of the Small eddy (region A) is much weaker than at depth. However, a variety of atmosphere–ocean exchange processes make near-surface fields difficult to interpret in terms of the underlying eddy structures.

DRIFTING BUOY TRAJECTORIES

During the experiment, several instrument arrays were deployed on drifting buoys. Interpretation of the drifter motions in terms of the eddy structure is difficult for a variety of reasons. To begin with, the arrays are not perfect tracers of fluid motion. The mass of the instrumentation is unevenly distributed through a depth interval (up to 2000 m) over which significant shear exists. The array is connected to a surface buoy that is subject to direct forcing from the wind. In addition, the realization of the eddy field depicted in the

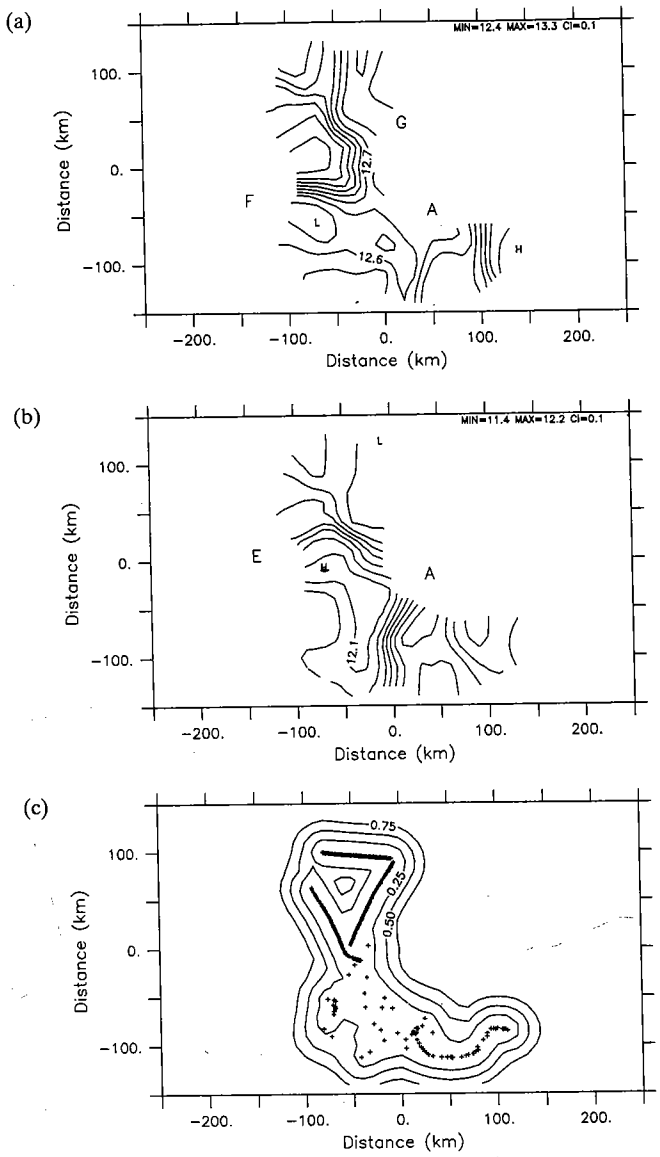

Fig. 14. Objectively analyzed temperature at (a) 25 m and (b) 200 m for the first data period in domain ABDE indicated in Fig. 7. The letters A, E, F and G show the locations of important features (see text). (c) Expected error map for the above analyses. Locations of observation points are indicated by plus signs.

preceding section is limited by the shallowness of the data; significant contributions to the total flow field certainly exist below the level of no motion necessarily chosen. Finally, the drifter trajectories result from a continuously evolving velocity field. That is, the pattern of currents can change significantly during the deployment. This is of particular concern in an area where several features are present and interacting. Therefore it is not reasonable to

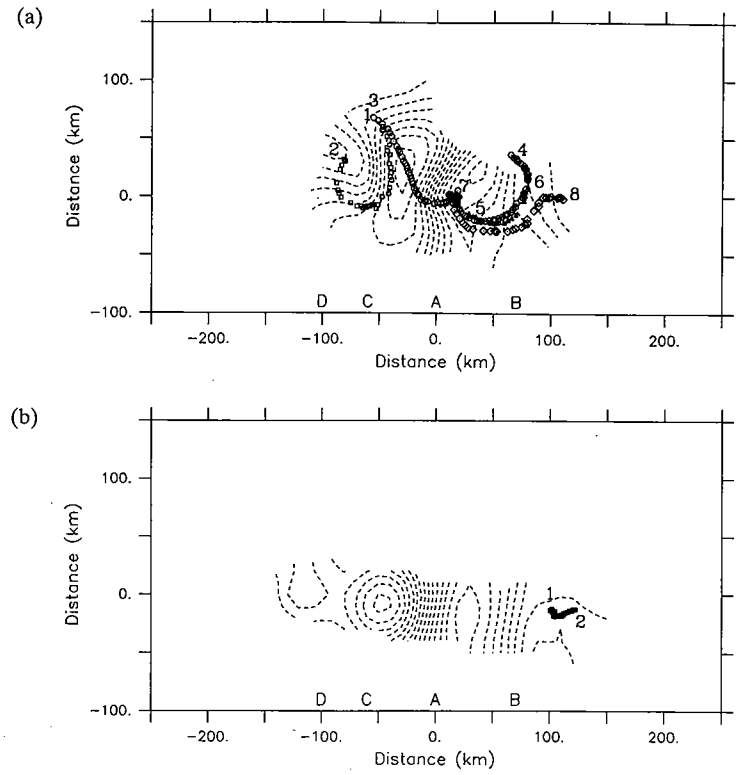

Fig. 15. Trajectories of the drifting instrument arrays overlayed on dynamic height fields for the first (a) and second (b) hydrographic data analysis periods. Numerals indicate deployment and recovery locations (see text).

expect that the drifter motions will coincide exactly with synoptic realizations of the geostrophic flow.

The trajectories of the arrays deployed during the first hydrographic data analysis period are overlayed on the dynamic height field in Fig. 15a. The first drifter followed a trajectory almost opposite to what the objective analysis would suggest. This array was deployed by R.V. *Atlantis II* and drogued to 90 m. Launched in the northeastern quadrant of the westernmost cyclonic feature at location 1 on 24 April (day 114), it traced out an anticyclonic pattern until it was recovered at location 2 on 1 May (day 121). While it is not possible to definitively explain explicitly the drifter's motion, it is important to note that its deployment was very early in the first data period, before most of the hydrographic data that went into the objective analysis were collected. It is therefore possible that the anticyclone was located further to the west during this time. If the feature were displaced approximately 30–40 km, the drifter motion would be consistent with the eddy pattern.

Another array drogued to 2000 m was deployed from R.V. *Atlantis II* at roughly the same location (3) on 24 April. This instrument moved from the northwest to the southeast across the anticyclonic feature in region C. This behavior is not totally counter-intuitive because the array was drogued in the deep ocean and the anticyclone was a near surface feature confined to the upper 300 m (Fig. 13). The drifter then traversed the frontal region

between the anticyclone and the Small eddy and then was apparently entrained into the cyclonic flow of the Small eddy, where it was recovered at location 4 on 17 May (day 137). The R.R.S. *Discovery* deployed her 300 m drifter at location 5 on 13 May (day 133) and then picked it up at location 6 on 17 May. Its motion was quite similar to that of the R.V. *Atlantis II* drifter, generally coinciding with the cyclonic flow of the Small eddy. F.S. *Meteor* launched a 300 m drifting array at location 7 on 9 May (day 129). At first its movement was consistent with the geostrophic pattern inside the Small eddy. But toward the end of the deployment it moved eastward across the north–south front in region B until it was recovered at location 8 on 21 May (day 141).

Only one drifting array was deployed during the second hydrographic data analysis period. The R.V. *Atlantis II* launched her 2000 m array on 18 May (day 138) at location 1 (Fig. 15b). It moved slowly east, in the direction of the geostrophic flow, until it was recovered at location 2 on 1 June (day 152).

MESOSCALE BIOLOGICAL VARIABILITY

Preliminary results from remotely sensed measurements suggest significant biological variability associated with the eddy features. Airborne Oceanographic Lidar (AOL) on board the NASA P-3 aircraft was used to estimate the chlorophyll content of the surface ocean (SWIFT and HOGE, 1990; YODER *et al.*, 1993). The AOL is a blue-green laser that stimulates fluorescence from phytoplankton chlorophyll. A telescope focuses the return signal on a detector array that measures the return spectra (32 bands continuously covering the range 387–736 nm). Chlorophyll fluorescence signals are extracted from the spectra, yielding estimates of relative phytoplankton chlorophyll concentration (HOGE, 1988). The P-3 also carried a PRT-5 radiometer for infrared measurements to determine sea surface temperature (SST). The raw data were filtered (low-pass) and sub-sampled yielding SST and chlorophyll fluorescence signals with a spatial resolution of approximately 0.5 km along the flight path of the plane.

Structure functions and other analyses of AOL data collected in the vicinity of the 47°N station showed that chlorophyll length scales (which correspond to the diameter of features) ranged from 10 to 289 km (mean = 49 km), and temperature length scales ranged from 12 to 214 km (mean = 59 km; YODER *et al.*, 1993). Recall that the diameters of the three eddies (Big, Standard and Small) were approximately 100, 200 and 270 km, respectively. The smallest scales in both chlorophyll and temperature may reflect the effects of local upwelling events resulting from the internal dynamics of mesoscale features as suggested by WOODS (1988). The submesoscale upwelling feature that occurs in the numerical simulation presented in Section 7 has a scale of approximately 40 km. The larger scale variability may relate to differences between mean concentration in the eddy cores versus surrounding waters. For example, consider a representative flight track over the Standard eddy, indicated by the dashed line along 20°W in Fig. 3. The alongtrack fluorescence (Fig. 16) indicates that the sea surface chlorophyll content inside the eddy core was elevated by about a factor of two, which would be consistent with increased nutrient supply in the upper ocean resulting from uplifted density surfaces in a cyclonic vortex. The chlorophyll enhancement inside this feature also was observed in a SeaSoar section through the eddy (LOCHTE *et al.*, 1993). The chlorophyll values were 1.5–2 outside the eddy and 2.5–3 inside.

A Coastal Zone Color Scanner (CZCS) chlorophyll image from 1 May 1985 (Fig. 17)

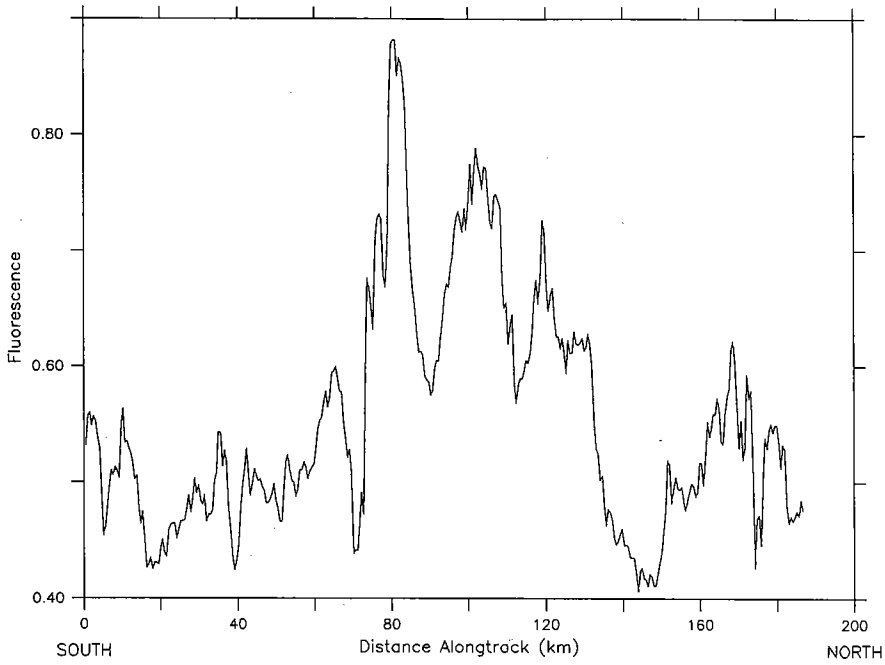

Fig. 16. Alongtrack fluorescence proceeding from south to north on the flight track indicated in Fig. 3 (dashed line).

illustrates two-dimensional spatial variability in near-surface chlorophyll in the study area (but not during the same spring as the present study). Structure functions calculated over the entire array from this and four other cloud-free CZCS images over the 48°N study area show dominant chlorophyll length scales ranging from 90 to 320 km (mean = 163 km). Smaller length scales (10–50 km) are also evident in individual lines extracted from the image (Fig. 18), but these smaller scales are lost during the averaging that occurs using data from the entire array (YODER *et al.*, 1987). No CZCS imagery is available for the spring of 1989 since the sensor stopped operating in 1986. However, chlorophyll length scales from five historical CZCS images centered on 48°N are consistent with predicted effects of mesoscale eddies in the study area in 1989 and with the maximum scales observed by aircraft.

ASSIMILATION INTO A DYNAMICAL MODEL FRAMEWORK

For the purposes of both physical and biological process studies, it is of interest to produce optimal estimates of the three-dimensional fields of interest as they evolve in time. The present approach consists of melding observations into a numerical model through assimilation techniques, so that the resulting fields are in agreement with the available data and dynamically adjusted across data sparse regions (ROBINSON and LESLIE, 1985). Dynamically consistent fields of secondary quantities of interest (such as vertical velocity) can be computed from the numerical solutions. In this assimilation the altimeter data are used to define the horizontal pattern of the fields over the large domain. The large

domain is necessary because the three eddies are interacting. A feature model technique (described below) is used for initialization throughout the water column. The choice of the free indices for the features are guided also by the available *in situ* data, as is the initialization for the near surface ocean.

In the simulation that follows, a coupled quasigeostrophic (ROBINSON and WALSTAD, 1987) and surface boundary layer model (WALSTAD, 1987; WALSTAD and ROBINSON, in press) has been initialized with the three vortices identified in the first eddy report. The initial fields have been constructed using vortex "feature models" originally developed for use in the Gulf Stream region (ROBINSON *et al.*, 1988). The technique allows for the generation of full water column fields from near surface information by making assumptions about the velocity structure of the features of interest. Estimates of the feature model parameters (eddy radii, swirl speeds and vertical shears) obtained from the altimetric and *in situ* observations therefore can be used to compute analytically the streamfunction and vorticity fields required for initialization of the quasigeostrophic model. In the axisymmetric feature model employed here, the velocity increases linearly out from the center to a radius of maximum velocity, beyond which it decays exponentially. There is linear shear in the vertical down to an assumed level of no motion at 2500 m. This vortex model was chosen to be consistent with both the present data and deeper historical data available in the region. In the surface boundary layer model, the initial buoyancy and temperature fields reflect the mean stratification for the region plus spatially varying perturbations due to the eddy features. The mixing layer depth is initially prescribed to be 80 m to reflect the well mixed pre-bloom condition.

The boundary conditions for the coupled model system are as follows. The horizontal boundary conditions are persisted throughout the integration. Surface fluxes of momentum and heat inferred from shipboard meteorological observations using standard bulk formulae are prescribed uniformly over the model domain at every time step. Fig. 19a–c shows the 10 m wind speed, the surface heat flux (composed of latent and sensible fluxes together with longwave back radiation) and net heat flux (the sum of the surface flux and shortwave solar radiation), respectively. The mean net heat flux is clearly into the ocean, as this quantity is dominated by the incoming shortwave solar radiation. However, there is noticeable heat loss from the ocean during the night. The observed mixed layer depth from CTD casts is shown in Fig. 19d along with simulated mixing layer depth.

The results of this model simulation are summarized in Fig. 20. In the initial condition (panel a) the three vortices show axisymmetric patterns of geostrophic velocity and vorticity at 50 m and temperature at 25 m. The mixing layer depth field is assumed to be spatially uniform at 80 m, which is intended to be representative of the conditions just prior to the beginning of the bloom. The vertical velocity is identically zero in the initial condition.

A period of light wind stress and relatively strong heat input into the ocean results in a shoaling of the mixing layer depth to about 26 m, which rapidly brings the model into agreement with the observations (Fig. 19d). Although slight, the spatial structure in the mixing layer depth field broadly coincides with the eddy features because of their perturbation of the stratification. Dynamical adjustment of the eddy features has initiated the vertical velocity field.

Over the next week the mixing layer depth generally deepens resulting from a small increase in wind stress and convection due to heat loss to the atmosphere during the night. For this time period the simulated mixing layer depth is slightly deeper than that observed.

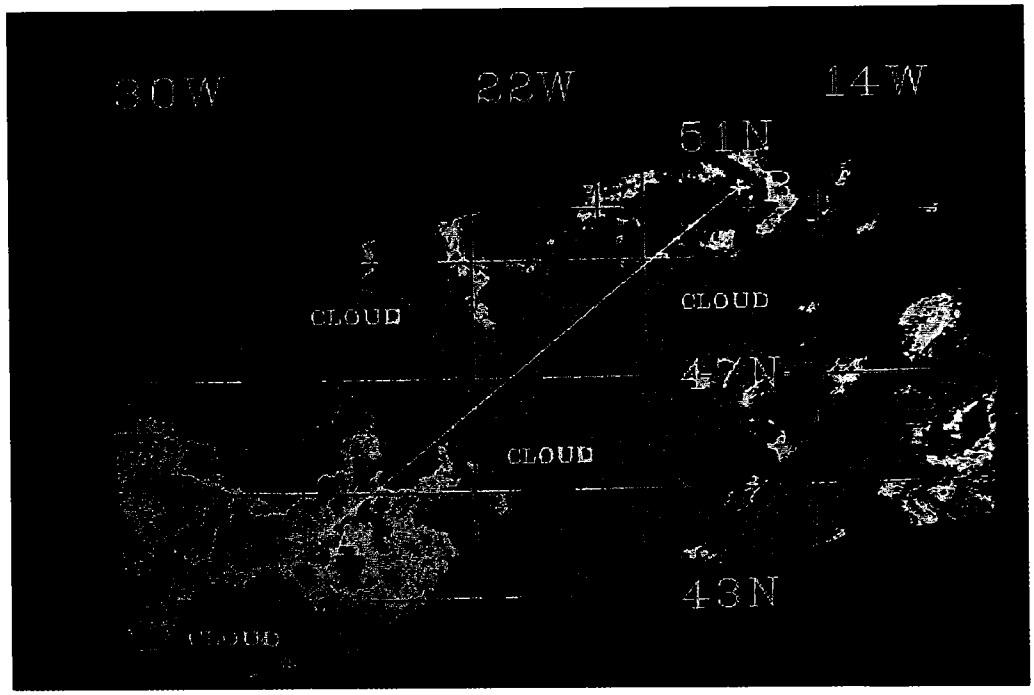

Fig. 17. Coastal Zone Color Scanner (CZCS) chlorophyll image over the 47°N study area on 1 May 1985. Chlorophyll concentration is color-coded with high concentrations (>1 mg m^{-3}) indicated by yellow and red and low concentrations (<0.5 mg m^{-3}) indicated by blue. Clouds are black. This representation shows the large-scale chlorophyll gradients. The mesoscale signal relevant to this study is evident in the data extracted along the line running southwest to northeast across the image (displayed in Fig. 18).

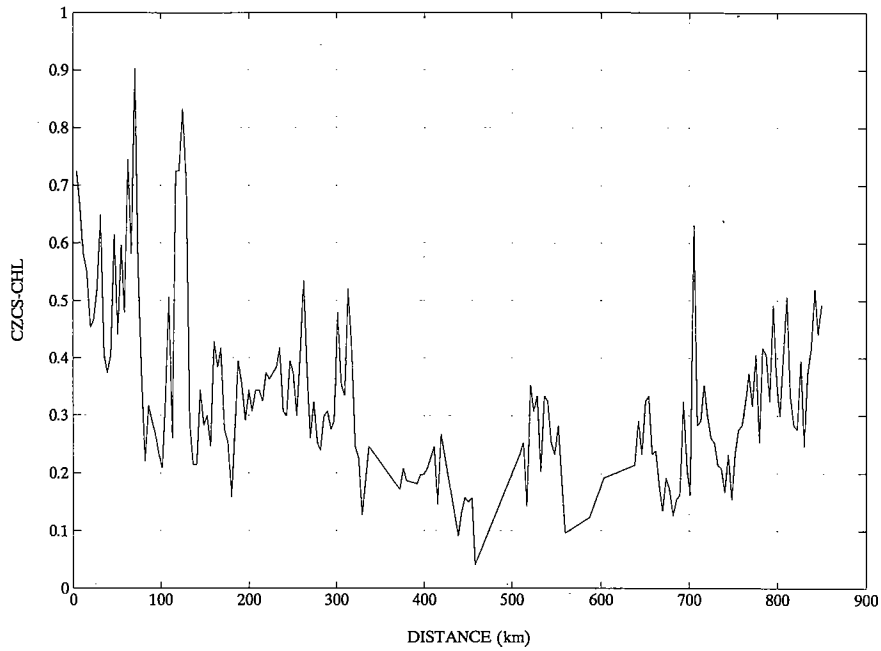

Fig. 18. CZCS chlorophyll concentrations extracted from the line indicated in Fig. 17.

The 50 m vorticity field shows that Big and Standard eddies have begun to interact and a submesoscale anticyclonic circulation has developed in between the Big and Small eddies.

From days 135.5 to 138.5 a decrease in wind stress and near cessation of nighttime heat loss allows the mixed layer to shoal to about 12 m, which is consistent with the data. The vertical excursions of the mixing layer depth have produced significant perturbations in the temperature field at 25 m through the generation of remnant layers. Significant deformation of the vorticity field of the Big eddy is evident as its southern flank has begun to meander somewhat. Localized patches of upwelling and downwelling have developed as a result of this dynamical process.

A storm on days 141–142 subsequently deepens the mixing layer to about 40 m, which is slightly shallower than the data indicate. Over this time period the patches of vertical velocity have developed further, with peak velocities reaching approximately 0.5 m day^{-1}. This is a quasigeostrophic submesoscale vertical transport process of the type described as a "hotspot" by Woods (1988). The interaction between the Big and Standard eddies has grown stronger, and Standard has now begun to interact with the Small eddy. In general, the vortices have evolved from their initial axisymmetric forms into a configuration that is consistent with the observations.

CONCLUSIONS

The physical environment in the vicinity of the 1989 JGOFS spring bloom experiment was quite complex. Three eddies, including an exceptionally large one, were identified via

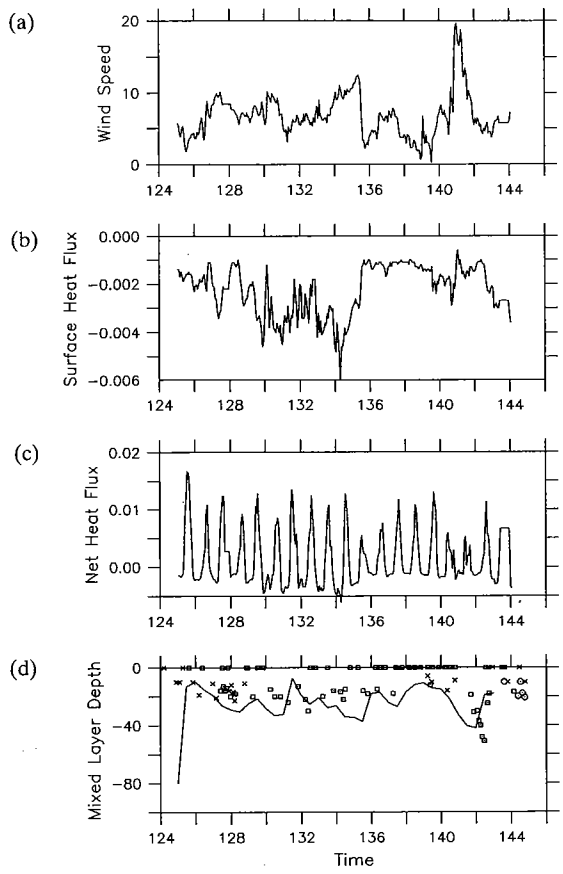

Fig. 19. (a–c) Ten meter wind speed and surface fluxes of heat used to force the model simulation (see text). (d) Observations of mixed layer depth from CTD casts (individual points) and simulated mixed layer depth (solid line). The mixed layer depth is reported to be zero when no clearly definable homogeneous layer exists in the temperature and salinity profiles. The abundance of zeros in the record reflects the fact that the CTD profiles were truncated above 10 m in some of the data sets.

Geosat altimetric data and some critical *in situ* data in real time and communicated to ships at sea for use in planning and executing experimental work. Analysis of the available hydrographic data validate the real-time estimates and help quantify the physical environment. Important submesoscale features include an anticyclone to the west of the Small

Fig. 20. Simulated fields of geostrophic velocity and vorticity at 50 m, mixing layer depth, temperature and vertical velocity at 25 m for (a) the initial condition (day 125); (b) day 127.5; (c) day 135.5; (d) day 138.5; and (e) day 141.5. The scale of the velocity vectors is shown for 18 cm s^{-1}. The minimum, maximum and contour interval for each contoured field are indicated. Dashed contours are used in regions where the fields are negative. Note that the contour interval changes for the mixing layer depth field.

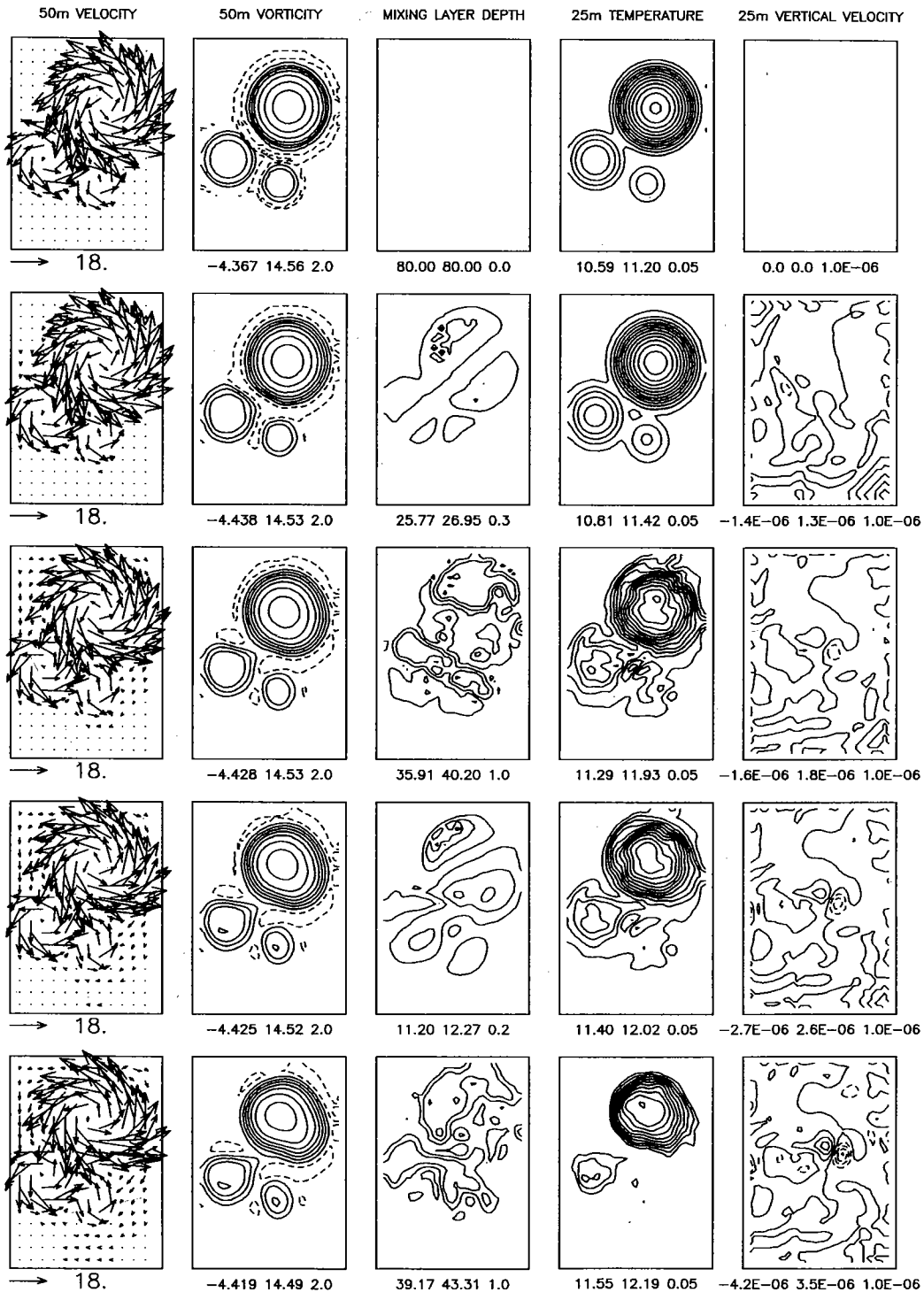
50m VELOCITY
50m VORTICITY
MIXING LAYER DEPTH
25m TEMPERATURE
25m VERTICAL VELOCITY
18.
-4.367 14.56 2.0
80.00 80.00 0.0
10.59 11.20 0.05
0.0 0.0 1.0E-06
18.
-4.438 14.53 2.0
25.77 26.95 0.3
10.81 11.42 0.05
-1.4E-06 1.3E-06 1.0E-06
18.
-4.428 14.53 2.0
35.91 40.20 1.0
11.29 11.93 0.05
-1.6E-06 1.8E-06 1.0E-06
18.
-4.425 14.52 2.0
11.20 12.27 0.2
11.40 12.02 0.05
-2.7E-06 2.6E-06 1.0E-06
18.
-4.419 14.49 2.0
39.17 43.31 1.0
11.55 12.19 0.05
-4.2E-06 3.5E-06 1.0E-06

eddy, an apparent secondary circulation inside the Small eddy, and upper ocean features arising from direct surface forcing and their interaction with the mesoscale. Assimilation of the observations into a dynamical model has been used to elucidate the deep ocean and near surface processes that combine to form the structures observed in the upper ocean. Under realistic atmospheric forcing, the mixed layer response is predominantly one-dimensional but significant eddy and smaller scale features are present. The numerical simulations also indicate a submesoscale region of relatively intense vertical transport associated with meandering induced by eddy interactions. Realistic four-dimensional field estimates derived from the dynamical model system are now being used as a framework for interdisciplinary study of coupled physical and biological processes. The apparent coincidence of scales in the North Atlantic for mesoscale features and concentrations of plankton, as evident from this work and the CZCS imagery, suggests a consistent biological response to a particular suite of physical phenomena and associated processes. The results reported in this paper demonstrate the power of altimetric remote sensing, supported by critical *in situ* data and data assimilation, to link, on the appropriate time and space scales, physical and biological features that reflect important processes influencing the magnitude, spatial extent, and temporal persistence of bloom processes in the open ocean.

Acknowledgements—A. R. R. and D. J. M. acknowledge ONR grants N00014-84-C-0461 and N00014-90-J-1593. D. J. M. was also supported under an ONR Graduate Fellowship. Some of the numerical simulations performed during this research effort were conducted at the San Diego Supercomputer Center under grant HVD200. H. D. acknowledges NSF Grant OCE89-04229. J. J. M. was supported by NSF grant OCE88-17830. S. P. and G. S. would like to thank the Deutsche Forschungsgemeinschaft projects ZE119/12-1/13-1 and PE378/1-2. J. Y. acknowledges NASA grant NAGW-1891. We also thank Drs Charles Kilgus and Julius Goldhirsh for help in making the Geosat data available, Dr Marlon Lewis of the NASA Ocean Biology Office for generously providing resources for a dedicated AXBT flight, Drs Gerhard Nee and Hans-Joachim Doescher of the Deutscher Wetterdienst Seewetteramt at Hamburg for providing shipboard meteorological observations, Drs. C. Langdon and J. Marra for providing drifter trajectories, the captains and crews of *Atlantis II*, R.R.S. *Discovery*, and F.S. *Meteor*, Aircraft Commander Virgil Rabine and the flight crew and AOL technical staff of the NASA P-3, and C. Garside for supplying some XBTs.

REFERENCES

ANGEL M. and M. FASHAM (1983) *Eddies and biological processes*, Chapter 22, Springer, Berlin.

ATHENA GROUP (in preparation) AthenA 88: an investigation of the regional structure of mesoscale fields in the Northeast Atlantic involved *in situ* observations and Geosat altimetry.

CALMAN J. (1987) Introduction to sea-surface topography from satellite altimetry. *Johns Hopkins APL Technical Digest*, **8**, 206–211.

CALMAN J. and L. MANZI (1989) Real-time satellite altimetry. *Johns Hopkins APL Technical Digest*, **10**, 380–384.

CARTER E. F. and A. R. ROBINSON (1987) Analysis models for the estimation of oceanic fields. *Journal of Atmospheric and Oceanic Technology*, **4**, 49–74.

DUCKLOW H. (1989) Joint Global Ocean Flux Study: the 1989 North Atlantic Bloom Experiment. *Oceanography*, **2**, 4–7.

GLENN S., D. PORTER and A. ROBINSON (1991) Validation of mesoscale dynamic topography from the Geosat altimeter and a synthetic geoid in the Gulf Stream meander and ring region. *Journal of Geophysical Research*, **96**, 7145–7166.

HANAWA K. and Y. YOSHIKAWA (1991) Re-examination of the depth error in XBT data. *Journal of Atmospheric and Oceanic Technology*, **8**, 422–429.

HOGE F. (1988) Oceanic and terrestrial lidar measurements. *Oceanic and Terrestrial Lidar Measurements*. Wiley, New York, pp. 409–504.

KUPFERMAN S., G. BECKER, W. SIMMONS, U. SCHAUER, M. MARIETTA and H. NIES (1986) An intense cold core eddy in the Northeast Atlantic. *Nature*, **319**, 474–477.

LEGROUPE TOURBILLION (1983) The Tourbillion experiment: a study of a mesoscale eddy in the eastern North Atlantic. *Deep-Sea Research*, **30**, 475–511.

LEVITUS S. and A. OORT (1977) Global analysis of oceanographic data. *Bulletin of the American Meteorological Society*, **59**, 1270–1284.

LOCHTE K. and O. PFANNKUCHE (1987) Cyclonic cold-core eddy in the eastern North Atlantic—II. Nutrients, phytoplankton and bacterioplankton. *Marine Ecology Progress Series*, **39**, 153–164.

LOCHTE K., H. DUCKLOW, M. FASHAM and C. STIENEN (1993) Plankton succession and carbon cycling at 47°N, 20°W during the JGOFS North Atlantic Bloom Experiment. *Deep-Sea Research II*, **40**, 91–114.

MITTELSTAEDT E. (1987) Cyclonic cold-core eddy in the eastern North Atlantic—I. Physical description. *Marine Ecology Progress Series*, **39**, 145–152.

NELSON D., J. MCCARTHY, T. JOYCE and H. DUCKLOW (1989) Enhanced near-surface nutrient availability and new production resulting from the frictional decay of a Gulf Stream warm-core ring. *Deep-Sea Research*, **36**, 705–714.

PORTER D., A. ROBINSON, S. GLENN and E. DOBSON (1989) The synthetic geoid and the estimation of mesoscale absolute topography from altimeter data. *Johns Hopkins APL Technical Digest*, **10**, 369–379.

ROBINSON A. (1986) Data assimilation, mesoscale dynamics and dynamical forecasting. In: *Advanced physical oceanographic numerical modelling*, J. O'BRIEN, editor, Reidel, Dordrecht, pp. 465–483.

ROBINSON A. and W. LESLIE (1985) Estimation and prediction of oceanic eddy fields. *Progress in Oceanography*, **14**, 485–510.

ROBINSON A. and L. WALSTAD (1987) The Harvard open ocean model: calibration and application to dynamical process, forecasting, and data assimilation studies. *Applied Numerical Mathematics*, **3**, 89–131.

ROBINSON A., M. SPALL and N. PINARDI (1988) Gulf Stream simulations and the dynamics of ring and meander processes. *Journal of Physical Oceanography*, **18**, 1811–1853.

ROBINSON A., S. GLENN, M. SPALL, G. GARDNER and W. LESLIE (1989) Forecasting Gulf Stream meanders and rings. *EOS*, **70**, 1464–1473.

SCHAUER U. (1989) A deep saline cyclonic eddy in the West European Basin. *Deep-Sea Research*, **36**, 1549–1565.

SWIFT R. and F. HOGE (1990) Surface layer phytoplankton chlorophyll and phycoerythrin pigment spatial distribution during the North Atlantic spring bloom 1989. *Transactions, American Geophysical Union*, **71**, 65.

WALSTAD L. J. (1987) Modelling and forecasting deep ocean and near surface mesoscale eddies: hindcasting and forecasting with, and coupling a surface boundary layer model to, the Harvard Quasigeostrophic Model. PhD thesis, Harvard University, Cambridge, MA 02138, Reports in Meteorology and Oceanography, No. 23.

WALSTAD L. and A. ROBINSON (in press) A coupled surface boundary layer–quasigeostrophic model, D.A.O.

WOODS J. (1988) Mesoscale upwelling and primary production. In: *Toward a theory on biological–physical interactions in the world ocean*, B. Rothschild, editor, Reidel, Dordrecht.

WUNSCH C. and E. GAPOSCHKIN (1980) On using satellite altimetry to determine the general circulation of the oceans with application to geoid improvement. *Reviews of Geophysics and Space Physics*, **18**, 725–745.

YODER J., J. AIKEN, R. SWIFT, F. HOGE and P. STEGMANN (1993) Spatial variability in near-surface chlorophyll *a* fluorescence measured by the airborne oceanographic lidar (AOL). *Deep-Sea Research II*, **40**, 37–53.

YODER J., C. MCCLAIN, J. BLANTON and L. OEY (1987) Spatial scales in CZCS-chlorophyll imagery of the southeastern U.S. continental shelf. *Limnology and Oceanography*, **32**, 929–941.

STATEMENT OF POLICY

Deep-Sea Research as interpreted by the Editor encompasses a wide variety of topics. The Editor therefore must rely on the comments and recommendations of referees competent in the several fields of the marine sciences as to a paper's scientific originality and its presentation. Acceptable topics include:

(1) the results of original scientific research
(2) theoretical work of evident oceanographic applicability
(3) the solution of some instrumental or laboratory problem with evidence of its successful use, and
(4) applications of oceanography.

Special issues dealing with particular concepts or areas are encouraged and will be published in Part II of *Deep-Sea Research.*

Papers dealing with research on continental shelves (water depths shallower than 100–200 m) in most cases should be submitted to our sister journal *Continental Shelf Research.*

Progress reports and review articles may be invited by the Editor but these are generally more appropriate for *Progress in Oceanography.* The Editor may also invite guest comment.

After receipt of a paper, every endeavour will be made to ensure prompt publication, if it is acceptable. Papers that are particularly timely or topical may receive accelerated editorial response and publication as Rapid Response Papers. However, the Editor reminds prospective authors that the most appropriate referee for their paper may be at sea.

Publishing, Subscription and Advertising Offices:

Pergamon Press Ltd, Headington Hill Hall, Oxford, OX3 0BW, UK (Tel: (0865) 794141; Fax (0865) 60285) or Pergamon Press Inc., 660 White Plains Road, Tarrytown, NY 10591-5153, USA

Microform and back issues

Back issues of all previously published volumes, in both hard copy and on microform, are available direct from Pergamon Press offices.

The Item-Fee Code for this publication is: 0967-0645/93 $5.00+0.00.